

Accepted Article Preview: Published ahead of advance online publication



Versatile biological imaging enabled by multimodal fluorescence-phase microscopy

Wenshu Wang, Suyi Zhong, Ruijie Cao, Xiaoyu Bu, Shu Gao, Qianxi Liang, Yunzhe Fu, Xuantao Su, Meiqi Li, and Peng Xi

Cite this article as: Wenshu Wang, Suyi Zhong, Ruijie Cao, Xiaoyu Bu, Shu Gao, Qianxi Liang, Yunzhe Fu, Xuantao Su, Meiqi Li, Peng Xi. Versatile biological imaging enabled by multimodal fluorescence-phase microscopy. *Light: Advanced Manufacturing* accepted article preview 24 March, 2026; doi: 10.37188/lam.2026.042

This is a PDF file of an unedited peer-reviewed manuscript that has been accepted for publication. LAM are providing this early version of the manuscript as a service to our customers. The manuscript will undergo copyediting, typesetting and a proof review before it is published in its final form. Please note that during the production process errors may be discovered which could affect the content, and all legal disclaimers apply.

Received 9 September 2025; revised 21 March 2026; accepted 24 March 2026;
Accepted article preview online 24 March 2026

Versatile biological imaging enabled by multimodal fluorescence-phase microscopy

Wenshu Wang^{1, †}, Suyi Zhong^{1, †}, Ruijie Cao^{1, †}, Xiaoyu Bu², Shu Gao¹,
Qianxi Liang¹, Yunzhe Fu¹, Xuantao Su³, Meiqi Li^{4, *}, and Peng Xi^{1, *}

¹ Department of Biomedical Engineering, National Biomedical Imaging Centre, College of Future Technology, Peking University, Beijing, 100871, China

² Key Laboratory of Analytical Science and Technology of Hebei Province, College of Chemistry and Material Science, Hebei University, Baoding, 071002, China

³ School of Integrated Circuits, Shandong University, Jinan, 250101, China

⁴ School of Life Sciences, Peking University, Beijing, 100871, China

† Equal Contribution.

[*lmeiqi@pku.edu.cn](mailto:lmeiqi@pku.edu.cn)

[*xipeng@pku.edu.cn](mailto:xipeng@pku.edu.cn)

Abstract

High-resolution, high-throughput, and minimally invasive imaging is in increasing demand in modern biomedical research. However, conventional single-modality optical microscopy often fails to satisfy these requirements, which limits its broader applicability. In this paper, we present a highly integrated multimodal fluorescence-phase microscopy (MFPM) system. By leveraging illumination pattern encoding, a unified wide-field detection configuration, and a highly integrated computational algorithm, MFPM achieves five imaging modes: optical-sectioning structured illumination microscopy (OS-SIM), super-resolution structured illumination microscopy (SR-SIM), polarisation dipole analysis, fast differential phase contrast (fDPC), and quantitative differential phase contrast (qDPC) imaging. By incorporating dark channel prior-based background removal, MFPM achieves enhanced optical-sectioning capability and improved imaging depth, whereas the frame-reduction reconstruction strategy enables a higher imaging speed. Consequently, the system requires only ten raw frames to reconstruct multidimensional information. In particular, DPC naturally complements SIM in terms of resolution and spatiotemporal throughput. This integrated platform enables co-registered multimodal imaging for diverse biomedical applications, including the subcellular visualisation of U2OS cells, quantitative auxiliary diagnosis of pathological tissue sections, and functional analysis of zebrafish heartbeats. With its compact design, multidimensional imaging capabilities, and strong biocompatibility, MFPM offers a unified solution for structural and functional imaging across biological scales. Its scalability toward intelligent event-triggered imaging, high-throughput acquisition, and virtual staining integration makes it a promising platform for next-generation automated biomedical imaging.

Keywords: Multimodal imaging, Super-resolution, Quantitative phase imaging, Structured illumination microscopy

1 Introduction

2 With the continuous advancement of biomedical research, single-modality optical
3 microscopy has shown inherent limitations^{1, 2}, as it cannot simultaneously satisfy the
4 increasing demands for high-resolution, high-throughput, and minimally invasive
5 imaging, thereby restricting its broader applications in areas such as drug screening³
6 and organ atlas construction⁴. Multimodal microscopy leverages the complementary
7 advantages of different imaging modalities and enables flexible switching according to
8 specific imaging requirements⁵⁻⁷, thus facilitating intelligent tasks such as high-
9 throughput screening⁸ and event-triggered acquisition⁹. Owing to these advantages, it
10 has emerged as a key direction for next-generation optical microscopy.

11 Optical microscopy techniques can be divided into two main categories: labelled
12 and label-free techniques. Among the labelled techniques, structured illumination
13 microscopy (SIM) has become widely used because of its super-resolution capability
14 and low phototoxicity¹⁰⁻¹⁷, which make it suitable for long-term and dynamic imaging,
15 including specific subcellular imaging in live cells. However, SIM has several inherent
16 challenges. First, because of its wide-field detection configuration, an out-of-focus
17 background is easily introduced when imaging thick samples, resulting in
18 reconstruction artifacts¹⁸. Second, the excitation of fluorescence signals requires
19 relatively high-intensity illumination, which can adversely affect cell viability during
20 prolonged imaging. Additionally, SIM typically requires nine raw images for
21 reconstruction, and its effective illumination region is confined to the coherence area of
22 the excitation beam, leading to limited imaging speed and field of view (FOV), and
23 constraining its applicability for large-scale and high-throughput scenarios¹⁹.

24 In the field of label-free imaging, differential phase contrast (DPC) has attracted
25 increasing interest in recent years owing to its high cost-effectiveness and excellent
26 optical compatibility²⁰⁻²². Unlike fluorescence imaging, which relies on specific
27 labelling, DPC provides rich global structural information for an entire specimen
28 without requiring labelling. It only requires replacing the light source of traditional
29 bright-field (BF) microscopy with a programmable LED array to extract phase

30 information via multi-angle illumination^{22, 23}. Furthermore, the illumination intensity
31 required for DPC is relatively low, resulting in negligible phototoxicity and minimal
32 disturbance of the biological state. Moreover, DPC employs global illumination, and its
33 FOV is not constrained by optical modulation devices, enabling a larger imaging area
34 under the same objective lens. Because of its simple optical configuration and strong
35 system scalability, DPC is naturally complementary to SIM in terms of resolution and
36 spatiotemporal throughput, making it ideal for constructing highly integrated and
37 biofriendly multimodal imaging systems.

38 Based on these considerations, we propose an integrated multimodal fluorescence-
39 phase microscopy (MFPM) system that seamlessly combines DPC and SIM into a
40 unified wide-field detection architecture. This system provides a low-cost and excellent
41 biocompatibility platform that supports high-throughput acquisition across
42 fluorescence, polarisation, and phase dimensions. Through incorporating the dark
43 channel prior-based background removal algorithm^{24, 25} for SIM preprocessing and the
44 frame-reduction strategy²⁶ to reduce the number of raw SIM images, only ten raw
45 frames are required to achieve five distinct reconstruction modes: optical sectioning
46 structured illumination microscopy (OS-SIM), super-resolution structured illumination
47 microscopy (SR-SIM), polarisation dipole analysis, fast DPC (fDPC), and quantitative
48 DPC (qDPC) imaging. The system is highly integrated with a space-efficient design,
49 occupying only 60 cm × 60 cm, which facilitates its rapid deployment in laboratory and
50 clinical settings. In practical applications on various biological samples, MFPM
51 synergistically combines high resolution with a large FOV, offers multiscale
52 adaptability and excellent biocompatibility, and provides complementary structural and
53 dynamic information in a single unified platform through system-level integration of
54 established modalities, such as DPC, SIM, and orientation mapping. Robust system-
55 level integration enables capabilities that no individual modality can achieve, making
56 it a cost-effective, multimodal imaging solution for biomedical research.

57 **Methods**

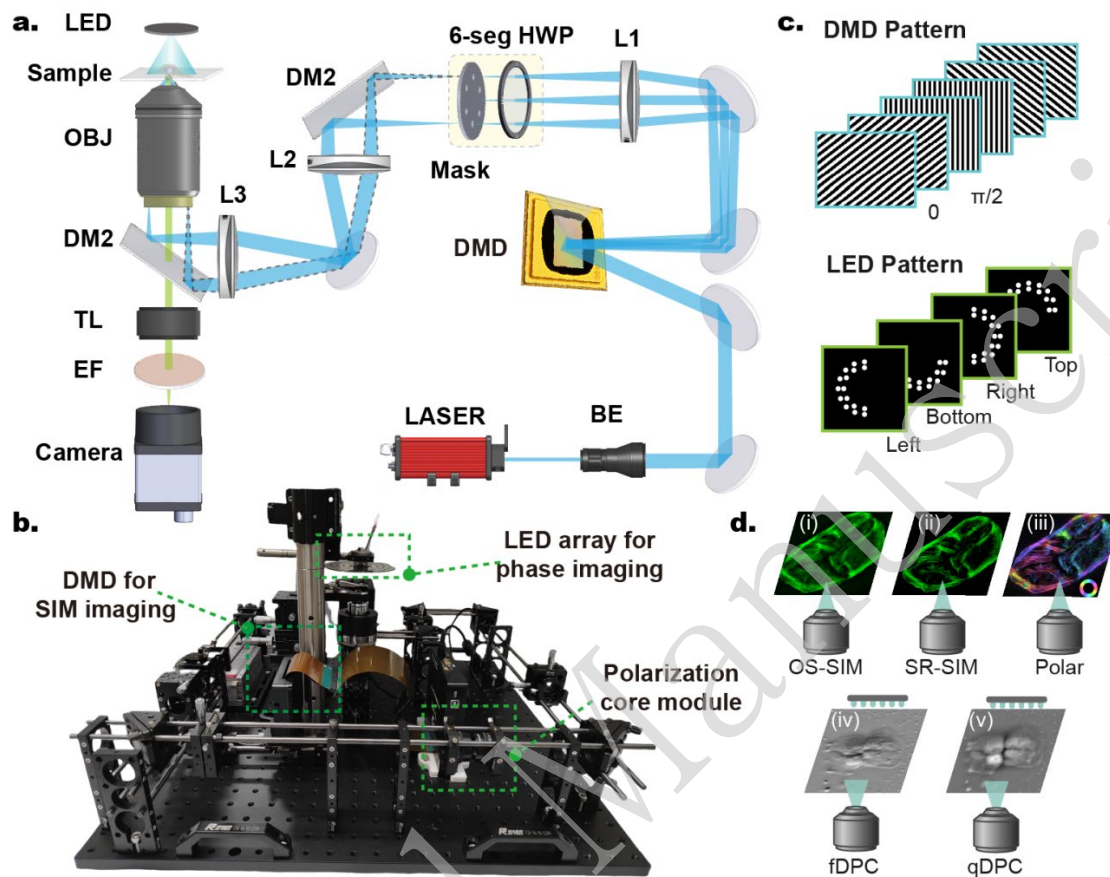
58 **System configuration**

59 In this study, a highly integrated multimodal fluorescence-phase system was
60 established, as illustrated in Figs. 1a, b. The system architecture combines a coherent
61 structured illumination module for fluorescence excitation with a programmable
62 partially coherent LED illumination module for label-free imaging while utilising a
63 unified detection optical path for signal collection across both modalities. This design
64 retains the high compatibility of wide-field detection within a compact 60 cm × 60 cm
65 footprint (Fig. 1b).

66 For the fluorescence illumination optical path, a 561 nm laser is expanded using a
67 beam expander (GBE10-A, Thorlabs) and directed onto a digital micromirror device
68 (DMD, F6500 Type-A, Fldiscovery Technology) at an incident angle of 24°. When
69 periodic fringe patterns are sequentially loaded into the DMD, as shown in Fig. 1c,
70 multiple diffraction orders are generated. The 0th and ±1st diffraction orders are
71 collected by an achromatic lens (L1, AC254-300-A-ML, Thorlabs) and focused onto a
72 custom-designed spatial mask, with hole diameter of 400 μm. This mask acts as a spatial
73 filter by blocking the 0th-order beam and selectively transmitting the ±1st-order beams
74 from three predefined directions. A six-sector half-wave plate (AHWP25-VIS-A-6P-M,
75 LBTEK) is used to ensure that the ±1st-order beams exhibit azimuthal polarisation
76 states depending on the direction. Owing to the coherence of the laser source, these
77 beams interfere at the focal plane of the objective lens, forming structured illumination
78 patterns on the sample.

79 The label-free illumination module consists of a cost-efficient, programmable
80 LED array controlled by a microcontroller (DFRduino Mega 2560, DFRobot). Because
81 the DPC technique uses transmitted illumination, a LED array is placed above the
82 objective lens. By adjusting the vertical distance between the LED array and the sample,
83 the illumination numerical aperture (NA) can be tuned to match that of the imaging
84 objective lens for optimal imaging conditions (detailed adjustment strategies are
85 provided in Supplementary Note 6). Because each LED can be controlled individually,
86 flexible illumination patterns can be generated electronically without mechanical
87 movement. In the DPC imaging mode, asymmetric illumination patterns (such as semi-
88 circular or semi-ring illumination) are encoded to modulate the spatial frequency

89 content of the sample, thereby enhancing the image contrast, the LED patterns are
 90 shown in Fig. 1c.



91

92 **Fig. 1. System Design and Multimodal Imaging Modes of MFPM.** **a.** Optical schematic of the MFPM
 93 system. L: lens, 6-seg HWP: six-sector half-wave plate, DM: dichroic mirror, OBJ: objective lens, TL: tube
 94 lens, EF: emission filter, DMD: digital micromirror device, BE: beam expander. **b.** Experimental layout of the
 95 imaging system. Core modules for different imaging modalities are outlined with green dashed boxes. **c.**
 96 Modulation patterns loaded into DMD and programmable LED array. **d.** Supported imaging modes of MFPM,
 97 including OS-SIM, SR-SIM, polarisation dipole analysis, fDPC, and qDPC imaging.

98 The two illumination modalities share a unified wide-field detection pathway.
 99 Through the combination of an emission filter (ET600/50M, Chroma) and dichroic
 100 mirror (ZT561rdc, Chroma), the system can obtain information from two distinct
 101 illumination modes using a single sCMOS camera (Dhyana 400BSI, Tucsen) with a
 102 2048×2048 pixel array. Based on a highly integrated configuration, five different
 103 imaging modes are supported by algorithmic reconstruction: OS-SIM, SR-SIM,
 104 polarisation dipole analysis, fDPC, and qDPC imaging, as illustrated in Fig. 1d. Owing
 105 to the limitations of camera read-out and synchronisation switching, we recommend a
 106 time interval of 15 ms or more for acquiring raw images in all five modes of imaging.

107 Refer to [Supplementary Note 4](#) for detailed experimental results.

108 **Multimodal reconstruction**

109 As mentioned earlier, the proposed MFPM system acquires multi-dimensional
110 information from only ten raw images. The shared detection path between SIM and
111 DPC ensures precise spatial registration for co-imaging, eliminates alignment artefacts,
112 and enhances data utilisation efficiency. A flowchart of the algorithm is shown in [Fig.](#)
113 [2a](#).

114 Both DPC and SIM employ illumination encoding and inverse-problem-based
115 decoding in their reconstruction processes. These techniques utilise multiple modulated
116 illumination patterns to encode distinct spatial frequency components of a sample into
117 an observable frequency band, followed by spectrum fusion or deconvolution for high-
118 fidelity reconstruction. Consequently, they share a unified computational reconstruction
119 framework using illumination encoding and model-based reconstruction. However,
120 these two methods aim to recover different information characteristics: DPC focuses on
121 retrieving phase distributions, whereas SIM targets higher-spatial-frequency
122 components of the fluorescence intensity beyond the diffraction limit. Consequently,
123 the physical models and reconstruction details differ. For qDPC reconstruction, raw
124 intensity images are captured under pairs of complementary asymmetric illuminations
125 generated by the programmable LED array. Each pair encodes the phase gradient along
126 opposite directions, and the qualitative phase gradient of the fDPC can then be retrieved
127 from only two corresponding raw images (e.g. I_L and I_R , which denote the images
128 captured under left and right illumination directions, respectively) at a very high
129 processing speed via differential normalization^{21, 22}:

$$130 \quad I_{DPC} = \frac{I_L - I_R}{I_L + I_R} \quad (1)$$

131 Similarly, another illumination pair is used to obtain the gradient in the orthogonal
132 direction. By utilising two or more raw image sets from orthogonal directions, isotropic
133 phase information can be reconstructed^{23, 27}. We then apply the Tikhonov regularisation
134 method to solve the inverse problem stably using an appropriate regularisation
135 parameter α_{DPC} :

$$136 \quad \phi(\mathbf{r}) = \mathbf{F}^{-1} \left\{ \frac{\sum_j [H_j^*(\mathbf{u}) \cdot \mathbf{F} \{I_j(\mathbf{u})\}]}{\sum_j |H_j(\mathbf{u})|^2 + \alpha_{\text{DPC}}} \right\} \quad (2)$$

137 where $\mathbf{F} \{I(\mathbf{u})\}$ represents the frequency spectrum of the raw frame, H represents the
 138 phase transfer function (PTF), \mathbf{u} denotes the spatial frequency coordinates, $*$ is the
 139 conjugate symbol, $\mathbf{F}^{-1}\{\cdot\}$ represents the inverse Fourier transform, and j represents
 140 the number of original images. Note that the reconstruction process relies on a weak-
 141 scattering approximation. Therefore, only the samples that satisfy this condition can
 142 yield relatively accurate results. For a detailed derivation of the DPC phase
 143 reconstruction algorithm, please refer to [Supplementary Note 1 and Fig. S1](#).

144 For the OS-SIM mode, we use two raw images and perform reconstruction using
 145 the HiLo algorithm^{28, 29}. The MFPM system further performs frame-reduction
 146 reconstruction and polarisation analysis to improve the imaging speed of the SR-SIM
 147 and resolve the dipole orientation. Therefore, we acquire only six raw images to achieve
 148 SR in this paper: two phase-shifted patterns for each of three stripe directions (with a
 149 phase difference of π). To mitigate out-of-focus background interference in thick
 150 samples caused by the wide-field detection hardware implementation of SIM, we use
 151 dark channel prior-based background removal algorithms, termed Dark sectioning, as
 152 the preprocessing step of SIM imaging. This algorithm separates the low- and high-
 153 frequency components in the Fourier domain. Through the application of dark channel
 154 processing to the low-frequency component, background contributions can be
 155 effectively suppressed²⁴.

156 Subsequently, a least-squares reconstruction²⁶ is conducted to reduce the number
 157 of reconstruction frames. Thus, the background-removed fluorescence distribution can
 158 be expressed as $D'_{\theta,\varphi}(\mathbf{r}) = [S(\mathbf{r}) \cdot I_{\theta,\varphi}(\mathbf{r})] \otimes h(\mathbf{r})$, and its frequency-domain
 159 representation becomes $D'_{\theta,\varphi}(\mathbf{k}) = [S(\mathbf{k}) \otimes I_{\theta,\varphi}(\mathbf{k})] \cdot h(\mathbf{k})$, where $S(\mathbf{r})$ and $I_{\theta,\varphi}(\mathbf{r})$
 160 are the sample and illumination distributions, respectively, and $h(\mathbf{r})$ is the point
 161 spread function. Using mutual correlation parameters, the frequency components across
 162 all illumination angles θ and phases φ are extracted. The frequency domain
 163 expression of the structured light modulation process can be obtained as

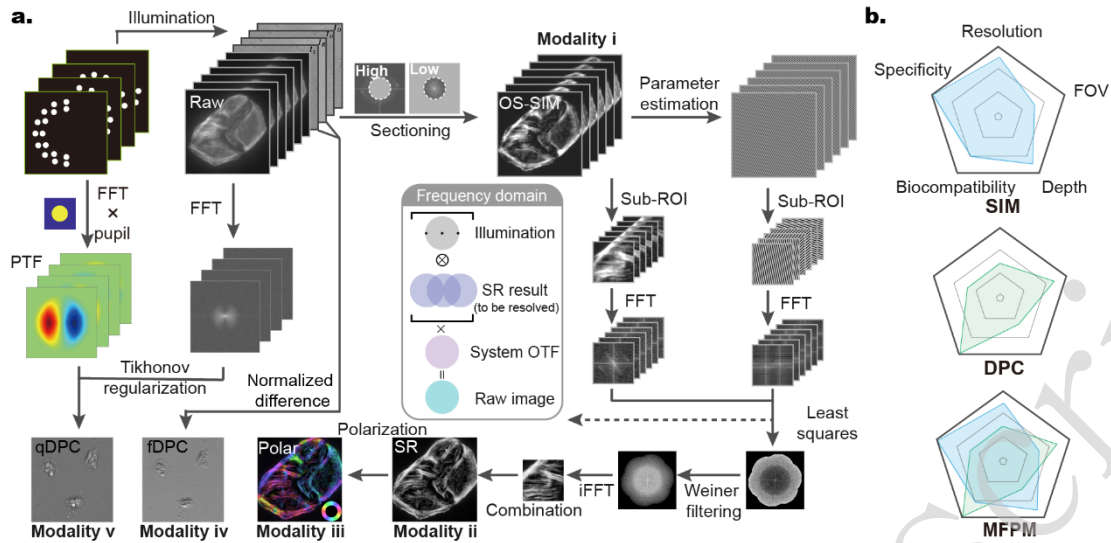
$$164 \quad \mathbf{d}' = \mathbf{M} \cdot \mathbf{S} \quad (3)$$

165 where \mathbf{d}' denotes the combination of known raw image frequency-domain pixels
 166 $D'_{\theta,\varphi}(\mathbf{k})$, \mathbf{M} is the result of multiplying the optical transfer function $H(\mathbf{k})$ by the
 167 estimated illumination stripes, and \mathbf{S} is the pixel combination of the SR image to be
 168 obtained. Subsequently, a Weiner filter is applied and the final spectrum of the SR
 169 image is transformed into the spatial domain. To accelerate computation, we separate
 170 the image into small patches for the acceleration of computation. Note that despite using
 171 only six raw images for super-resolution reconstruction, the final result is comparable
 172 to that achieved with nine frames (see [Supplementary Note 5](#) for details). Furthermore,
 173 owing to the Dark sectioning preprocessing applied to the raw image, the reconstructed
 174 SIM achieves an increased imaging depth.

175 To further resolve the dipole orientation information, we obtain a wide-field (WF)
 176 image $W_{\theta}(\mathbf{r})$ by superimposing two phase-shifted fluorescence images, where the
 177 dipole response to polarised illumination follows $g_{\theta_i}(\mathbf{r}) = [1 + \cos(2\theta_{pi} - 2\rho)] / 2$ ³⁰⁻³².
 178 The orientation can then be determined by solving the following linear system:

$$179 \quad \begin{bmatrix} W_{\theta_1} \\ W_{\theta_2} \\ W_{\theta_3} \end{bmatrix} = \frac{1}{2} \begin{bmatrix} 1 & \cos 2\theta_{p1} & \sin 2\theta_{p1} \\ 1 & \cos 2\theta_{p2} & \sin 2\theta_{p2} \\ 1 & \cos 2\theta_{p3} & \sin 2\theta_{p3} \end{bmatrix} \begin{bmatrix} 2I_{DC} \\ I_{AC} \cdot \cos 2\rho \\ I_{AC} \cdot \sin 2\rho \end{bmatrix} \quad (4)$$

180 where θ_{pi} is the polarisation angle in each illumination, ρ is the dipole of the
 181 fluorescence orientation, and I_{DC} and I_{AC} are the unchanged and changed
 182 components of the polarisation modulation, respectively. The detailed implementation
 183 of fluorescence reconstruction and a comparison of the polarisation-resolved methods
 184 are described in [Supplementary Note 2](#) and [Supplementary Tables](#).



185

186 **Fig. 2 Multimodal image reconstruction process and comparison of modality performance radar chart.**
 187 **a.** Image reconstruction workflow in MFPM imaging. The grey box in the middle represents the frequency
 188 domain representation of the process of super-resolution information imaging of the sample. **b.** Radar chart of
 189 SIM, DPC, and MFPM on different performance criteria.

190 We conducted a comprehensive performance evaluation of the MFPM by
 191 comparing SIM, DPC, and MFPM across five key metrics using radar charts: resolution,
 192 FOV, specificity, biocompatibility, and imaging depth. As illustrated in Fig. 2b, the
 193 MFPM system demonstrated remarkable synergistic advantages by combining the
 194 super-resolution and specificity of SIM with the large FOV and rapid imaging
 195 characteristics of DPC. Specifically, our actual measurements showed that the FOV of
 196 the phase modality was approximately 11.5 times that of the fluorescence modality (See
 197 [Supplementary Note 4](#) for detailed results). Benefiting from the frame-reduction
 198 algorithm and integrated reconstruction of phase and polarisation information, MFPM
 199 significantly enhances both information throughput and content richness within the
 200 same acquisition time. More importantly, the ability to switch between imaging tailors
 201 to different scenarios significantly improves the biocompatibility of MFPM. This
 202 multimodal integration strategy not only overcomes the inherent limitations of
 203 conventional single-mode microscopy but also establishes a framework for high-
 204 throughput, multidimensional biological imaging, laying the foundation for more
 205 versatile biological applications.

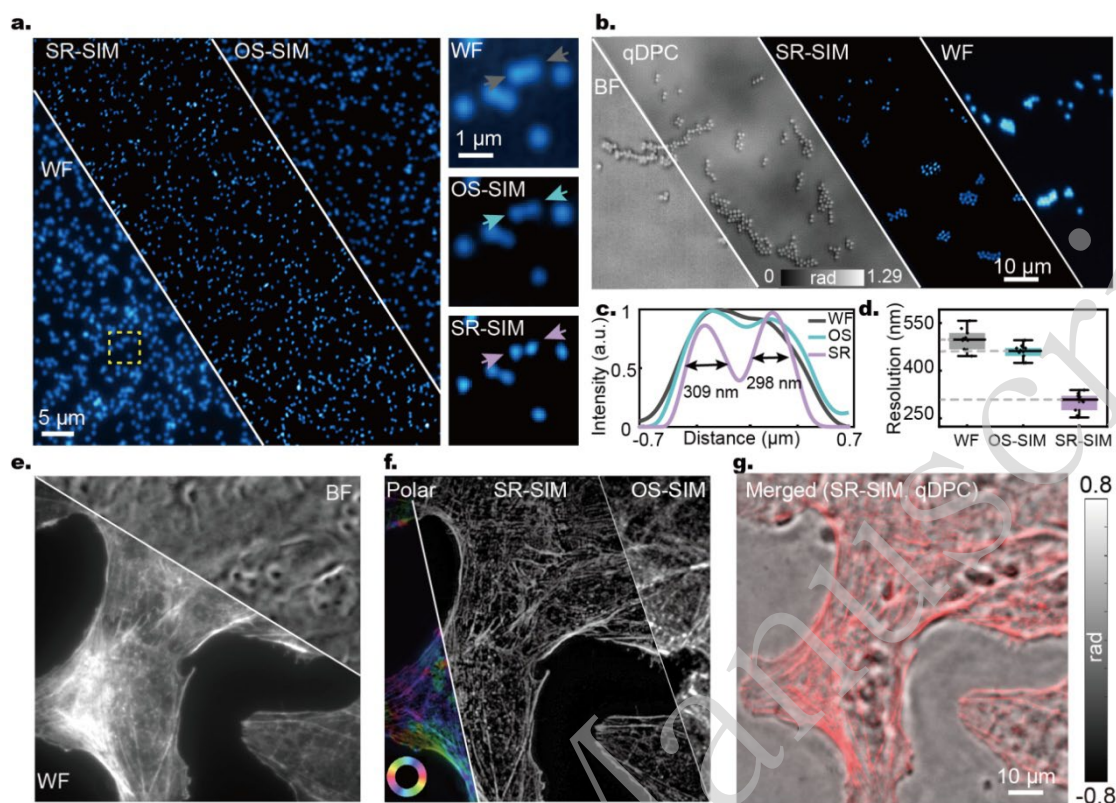
206 Results

207 **Imaging performance verification and multimodal imaging of subcellular**
208 **structures**

209 MFPM involving five modes can provide multidimensional information jointly:
210 optical sectioning and high-resolution fluorescence information (OS-SIM and SR-SIM),
211 large-FOV label-free panoramic cellular information (fDPC and qDPC), and
212 orientation-dependent information (polarisation dipole analysis). To validate the
213 fluorescence super-resolution capability and quantitative phase reconstruction
214 performance of the system, we first imaged 1 μm fluorescent polystyrene beads using a
215 20 \times /0.8 NA objective lens. See [Supplementary Note 9](#) for the detailed preparation of
216 fluorescent polystyrene beads. As shown in [Fig. 3b](#), the reconstructed qDPC results
217 clearly resolved the densely clustered fluorescent beads that remain indistinguishable
218 in conventional BF images. Given that the fluorescent beads are composed of
219 polystyrene (refractive index $n = 1.59$), the theoretical maximum phase value of a 1 μm
220 bead is calculated to be $2\pi(n - n_0)d / \lambda = 0.72$ rad. The experimentally measured
221 phase difference between the centre and edge of the bead was approximately 0.71 rad,
222 indicating that the experimental results agreed well with the theoretical value.

223 Meanwhile, fluorescence SR-SIM reconstruction significantly improved the
224 spatial resolution compared with fluorescence WF microscopy. To assess this
225 improvement, we further imaged 100 nm fluorescent beads using a 40 \times /0.95 NA
226 objective lens ([Fig. 3a](#)). The SR reconstruction results achieved better resolution than
227 the WF and OS-SIM, breaking the theoretical diffraction limit of 392 nm calculated
228 based on the Rayleigh criterion. For two adjacent fluorescent beads, both WF and OS-
229 SIM failed to resolve them, whereas the fluorescence SR results could distinguish them
230 and full width at half maximum (FWHM) values of 309 and 298 nm, respectively ([Fig.](#)
231 [3c](#)). To ensure statistical reliability, we analysed the FWHM of 10 randomly selected
232 fluorescent beads, yielding an average SR resolution of 298 ± 29 nm (mean \pm standard
233 deviation), compared with 496 ± 33 nm for WF and 457 ± 22 nm for OS-SIM imaging,
234 as illustrated in [Fig. 3d](#). This represents an approximately 1.7-fold improvement in
235 resolution over conventional WF imaging. Note that the resolution of the WF was
236 slightly larger than the diffraction limit, and we concluded that the cause of this

237 degradation was spherical aberration resulting from the refractive index mismatch.



238

239 **Fig. 3 Comparison of MFPM results of fluorescent beads and subcellular structures under different**
 240 **imaging modes. a.** Comparison of WF, OS-SIM, and SR-SIM imaging results for 100 nm fluorescent beads
 241 using a 40×/0.95 NA objective lens. The figures on the right are the comparison of imaging results within the
 242 yellow dashed box in left images. **b.** BF, qDPC, fluorescence WF and SR imaging results of 1 μm beads using
 243 a 20×/0.8 NA objective lens. **c.** Intensity distribution of the arrowed region in a. **d.** Average resolution obtained
 244 by statistically analysing the imaging results of 10 randomly selected fluorescent beads from a. **e.** Comparison
 245 of BF and fluorescence WF imaging results using a 40×/0.95 NA objective lens. **f.** Fluorescence imaging results
 246 of polarization, SR-SIM, and OS-SIM. **g.** Multimodal integration of SR-SIM reconstruction results and qDPC
 247 imaging results. For fluorescence modes, the emission wavelength is 610 nm, and the centre wavelength of the
 248 LED used for phase imaging is 610 nm.

249 Consequently, the MFPM platform enables seamless multimodal imaging of both
 250 label-free and fluorescence-labelled structures within the same area of the sample,
 251 offering the potential for in-depth subcellular organelle analyses. In multimodal
 252 imaging, DPC imaging offers an outline of the global cellular morphology, whereas the
 253 fluorescence channel reveals subcellular features with enhanced resolution. We imaged
 254 U2OS cells stained with Alexa Fluor 568-phalloidin to visualise the filamentous actin.
 255 With a 40×/0.95NA objective lens, the phase image effectively provided panoramic
 256 structural information of the cell, whereas the fluorescence SR results provided more

257 specific and detailed spatial information. The SR imaging results were compared with
258 WF and OS-SIM methods, as shown in Figs. 3e, f. Quantitative analysis demonstrated
259 that the signal-to-background ratio of SR reached 9.19 dB, exceeding that of WF
260 imaging (7.34 dB). Fourier ring correlation (FRC)³³ analysis indicated that the SR
261 achieved a nearly 1.6-fold resolution enhancement (see Fig. S17).

262 Polarisation-resolved analysis was performed on the same dataset to extract the
263 dipole orientation information of the actin filaments. The resulting polarisation maps
264 complemented the structural details obtained from SR imaging and provided insights
265 into cytoskeletal alignment and anisotropy (Fig. 3f). Finally, we merged the qDPC and
266 SR-SIM fluorescence reconstructions to create a composite view combining the
267 morphological context with high-resolution and more detailed information,
268 highlighting the capability of MFPM to simultaneously capture multidimensional
269 subcellular information across different imaging modalities (Fig. 3g).

270 **Quantitative Multimodal Analysis for Pathological Tissue Classification**

271 Cervical cancer is one of the most prevalent malignancies affecting women
272 globally and poses a significant threat to their health and survival³⁴. In the diagnosis
273 and treatment of cervical tumours, surgical excision of the lesion tissue is typically
274 required for pathological evaluation. However, in the differential diagnosis of common
275 cervical lesions, particularly for distinguishing cervicitis (a benign condition) from
276 cervical cancer (a malignant tumour), traditional H&E staining, which is widely
277 recognised as the gold standard in clinical pathological diagnosis, relies heavily on
278 subjective interpretation by pathologists, introducing uncertainties and inter-observer
279 variability. To mitigate these limitations, we employed our MFPM system to acquire
280 fluorescence and phase information from standard cervical tissue sections with a
281 thickness of 5 μm . This approach leverages quantitative fluorescence intensity data
282 combined with nuclear features (nuclear density and count) derived from subsequent
283 cell segmentation analysis.

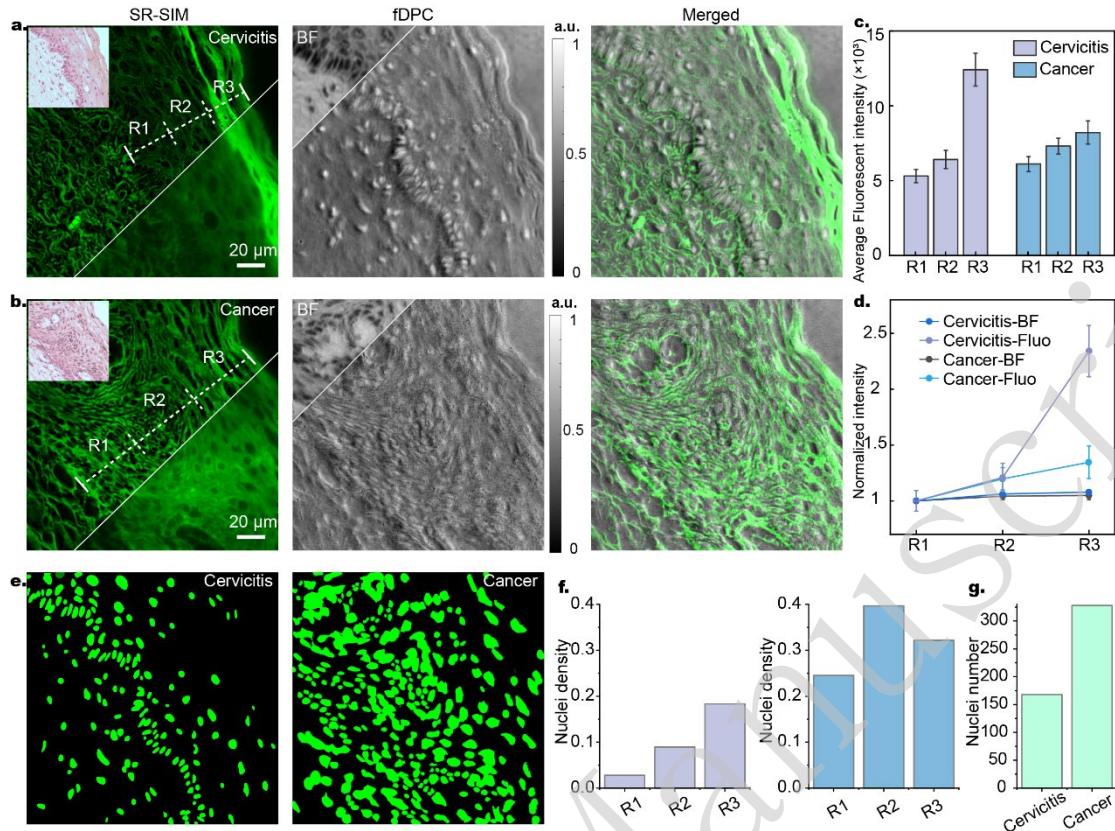
284 During the imaging process using a 20 \times /0.8NA objective, fDPC imaging was first
285 performed on cervicitis and cervical cancer tissue sections to quickly obtain the
286 corresponding gradient map. This mode was prioritised because of its large FOV and

287 imaging speed (requiring only two raw images), which enabled the efficient capture of
288 structural contour information across the sample. DPC observations revealed distinct
289 tissue architectures; cervical cancer tissues demonstrated weaker edge information,
290 reduced structural continuity, and a narrower phase variation range than benign
291 cervicitis tissues (Figs. 4a, b). Upon identification of suspicious regions using the large
292 FOV of DPC, fluorescence signal acquisition was performed. However, thick tissue
293 sections often introduce significant out-of-focus background light. Therefore, the use
294 of the dark-channel prior-based background removal algorithm significantly enhanced
295 the structural clarity of the fluorescence image. Figs. 4a, b present representative co-
296 registered results, showing the fluorescence SR images, fDPC images, and their merged
297 multimodal visualisation within identical regions of interest. The DPC images revealed
298 global cellular contours within the tissue. In contrast, SR-SIM resolved more detailed
299 structural features, including fine perinuclear distributions, that reflect subtle variations
300 related to cellular differentiation and malignancy. Together, these two modalities
301 provided complementary information that could not be obtained individually.

302 Quantitative analysis of fluorescence intensity within the epithelial regions of the
303 tissue sections was performed using SR fluorescence images. More than 20 line
304 segments were drawn traversing the epithelium perpendicularly and extending from the
305 basement membrane to the epithelial surface. The fluorescence intensity profiles along
306 these lines were determined. The epithelial thickness along each line was systematically
307 divided into three equal segments, Segments 1–3, corresponding to different
308 differentiation stages from the basal to the superficial layer. The average fluorescence
309 intensity within each segment was calculated for analysis, as shown in Fig. 4c. To
310 mitigate variations arising from technical factors, such as staining intensity, exposure
311 time, and tissue thickness, we normalised each individual fluorescence intensity profile
312 was by dividing all intensity values within a profile by the average intensity of its
313 corresponding Segment 1 (basal layer). The resulting normalised fluorescence intensity
314 profiles, along with the normalised BF intensity profiles for comparison, are shown in
315 Fig. 4d. The results indicated significant differences in the epithelial fluorescence
316 intensity distribution between cervicitis and cervical cancer specimens, whereas almost

317 no difference was observed in the intensity distribution of BF. Therefore, the
318 fluorescence intensity of the sample can objectively reflect whether the cervical tissue
319 section is malignant. Compared with cervical cancer tissues, cervicitis samples retained
320 significantly more fluorescence within the epithelium, with the highest intensity
321 localised in the cytoplasm of keratinocytes in the superficial epithelial layer. The
322 fluorescence intensity was the lowest in basal cells and progressively increased with
323 keratinocyte maturation and epithelial differentiation. These findings are consistent
324 with previous reports³⁵ and may be attributed to the accumulation of various keratins
325 and other proteins associated with mature keratinocytes³⁶.

326 To further quantify the nuclear morphological features for diagnostic
327 differentiation, we performed nucleus segmentation on the fDPC images of cervical
328 tissue sections using Cellpose SAM³⁷. Fig. 4e shows the results for cervicitis and
329 cervical cancer samples after the segmentation parameters were optimised. Cervical
330 cancer samples exhibited markedly higher nuclear densities than cervicitis samples. For
331 rigorous quantitative analysis, the nuclear density was calculated within three distinct
332 regions for each sample type (Fig. 4f). The results demonstrated a consistent trend:
333 across all three regions, cervical cancer tissues displayed a significantly elevated
334 nuclear density relative to cervicitis. This difference was most pronounced in region R2,
335 where the nuclear density of cervical cancer tissues peaked at 0.40 nuclei/pixel,
336 indicating increased cellular proliferation associated with malignancy. Additionally, the
337 total number of nuclei was compared among the groups, as shown in Fig. 4g. Cervical
338 cancer tissues exhibited more than twice the nuclear density of cervicitis tissues,
339 providing quantitative support for the observed differences in the nuclear distribution
340 between benign inflammatory and malignant neoplastic lesions. Collectively, these
341 findings, derived from the quantitative analysis of the data acquired using our MFPM
342 system, indicate that nuclear density and count serve as robust quantitative markers for
343 distinguishing cervical inflammatory conditions from neoplastic transformations.



344

345 **Fig. 4 Multimodal imaging and quantitative statistics result for cervicitis and cervical cancer using a**
 346 **20 \times 0.8 NA objective lens. a.** Multimodal imaging results for cervicitis. **b.** Multimodal imaging results for
 347 cervical cancer. **c.** Fluorescence intensity statistics under different regions. **d.** Fluorescence intensity
 348 normalization. **e.** Cell segmentation results for cervicitis and cervical cancer. **f.** Statistical results of nuclei density
 349 in different regions of cervicitis (left) and cancer (right). **g.** Results of cell nucleus counting in the same FOV for
 350 cervicitis and cervical cancer. The emission centre wavelength was 610 nm.

351 In summary, we demonstrated the feasibility of performing quantitative
 352 pathological analysis of standard tissue sections by integrating multimodal imaging,
 353 normalised image-processing pipelines, and nuclear analysis. This integrated approach
 354 provides a more objective and reproducible imaging-based framework for auxiliary
 355 diagnosis of cervical lesions. The analytical workflow which utilises fDPC imaging for
 356 the high-throughput screening of a large FOV, followed by SR fluorescence validation
 357 and detailed quantitative analysis of the regions of interest, further underscores the
 358 inherent advantages of our MFPM system. The key is the synergistic capability of the
 359 correlation between the overall structures and quantitative molecular or functional data.
 360 Furthermore, the complementary capabilities of the DPC and fluorescence imaging
 361 modalities within the MFPM platform were exemplified by additional results obtained

362 from mouse skin tissue sections (Figs. S14 and S15), as detailed in [Supplementary Note](#)
363 [7](#).

364 **Multimodal Imaging of Zebrafish Cardiac Function and Neutrophil Migration**

365 In pharmaceutical research, cardiotoxicity is one of the major factors contributing to
366 the early termination or delay in candidate drug development. Cardiotoxicity
367 assessment primarily relies on heart rate-related parameters, particularly heart rate
368 variability (HRV), which is widely recognised as a key biomarker of cardiac
369 arrhythmias³⁸. Consequently, accurate high-throughput quantification of heart rate and
370 HRV in model organisms such as zebrafish is essential to efficient drug screening and
371 toxicology. Commonly used methods for heart detection include electrocardiography
372 (ECG), image-based analysis software³⁹, and manual counting⁴⁰. However, these
373 methods often lack cross-validation mechanisms to verify the accuracy of heart rate
374 quantification, and manual counting is significantly affected by human factors in
375 arrhythmia detection, resulting in low efficiency and insufficient accuracy.

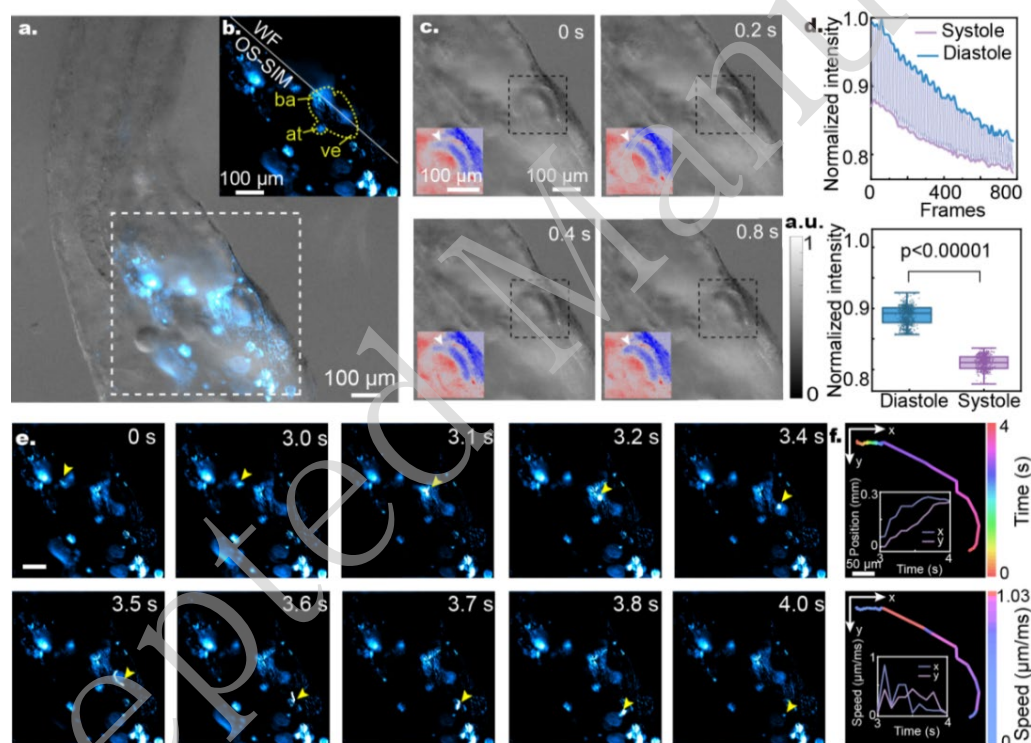
376 To overcome these constraints, the proposed MFPM system leverages its unique
377 multimodal capabilities. Exploiting the rapid pattern-switching capacity of its LED
378 array and DMD alongside our frame-reduction reconstruction algorithm, MFPM
379 enables synergistic cardiac imaging; DPC provides rapid global localisation of the
380 beating heart within seconds, whereas the simultaneously acquired fluorescence
381 delivers subcellular-resolution contractile dynamics. In this study, Tg (lyzC:Cherry)
382 transgenic zebrafish were used as the experimental model, and the detailed sample
383 preparation process is shown in [Supplementary Note 9](#). Combining DPC and
384 fluorescence imaging to cross-validate the results can significantly improve the
385 measurement accuracy of heart rate parameters (such as heart rate, heartbeat interval,
386 and rhythm fluctuation) while significantly reducing the time and labour demands
387 associated with manual analysis. Time series derived from intensity fluctuations in
388 sequential video frames, which reflected atrial and ventricular contractions, were
389 analysed to extract and quantify zebrafish heartbeat dynamics.

390 The synergistic multimodal workflow of our MFPM system offers significant

391 advantages. During the experiment, we used a 10×/0.3NA objective lens. The fDPC
392 imaging enabled rapid whole-organ screening, instantly locating the zebrafish heart
393 within seconds across a large FOV, and eliminating the need for manual searching.
394 Considering motion during the imaging process, we used agarose to embed juvenile
395 fish and the scale-invariant feature transform (SIFT)-based⁴¹ registration plugin in Fiji
396 for rigidity correction. More specifically, the fDPC images clearly captured the phase
397 gradient of the zebrafish heart throughout the beating cycle, revealing a periodic
398 contraction approximately every 0.4 s, corresponding to a heart rate of ~150 beats per
399 minute (bpm), which is consistent with the typical range (120–180 bpm) for zebrafish
400 at 72 h post-fertilisation (72 hpf)⁴², as shown in Figs. 5a, c. Subsequently, fluorescence
401 images were captured and OS-SIM results were reconstructed. After photobleaching
402 correction and image registration, the fluorescence intensity of the heart region shown
403 in Fig. 5b was further subjected to time-series statistics, with the original intensity
404 fluctuations depicted in Fig. 5d. During diastole, the heart chambers expand to
405 accommodate more labelled cells, resulting in stronger fluorescence. However, during
406 systole, the number of labelled cells decreases. Therefore, the periodic fluctuations in
407 fluorescence intensity faithfully represent the cardiac systole and diastole phases, with
408 intensity peaks corresponding to systole and troughs to diastole⁴². A t-test confirmed a
409 statistically significant intensity difference between the two states ($p < 0.00001$),
410 supporting its use in quantitative heartbeat characterisation. By analysing the intervals
411 between adjacent fluorescence peaks and applying Fourier transform analysis, we
412 determined the estimated heart rate was to be approximately 153 bpm. The high
413 concordance between the DPC-derived (~150 bpm) and fluorescence-derived (~153
414 bpm) heart rates provides an intrinsic cross-validation that is unattainable with single-
415 modality systems, significantly enhancing the reliability of HRV and arrhythmia
416 assessment. This framework significantly reduces the analysis time compared with
417 manual methods, providing unprecedented measurement confidence for efficient
418 cardiotoxicity screening.

419 Beyond cardiac dynamics, the MFPM platform enables the effective investigation

420 of neutrophil migration, which is a critical process in innate immunity. Neutrophils can
 421 rapidly respond to changes in the tissue microenvironment⁴³, and their dysfunction is
 422 closely associated with various inflammation-related diseases and deficiencies in innate
 423 immune defense⁴⁴, which makes the study of their migratory behaviour important. In
 424 zebrafish larvae, neutrophils predominantly reside within tissues, providing a valuable
 425 *in vivo* model for investigating their migration dynamics and functional responses in
 426 the tissue context. By leveraging the OS-SIM mode in the fluorescence module of the
 427 MFPM system, which offers excellent background suppression capabilities, we
 428 achieved precise tracking of neutrophil recruitment and damage response dynamics,
 429 which were previously challenging to capture using conventional microscopy.



430

431 **Fig. 5 Multimodal heart rate monitoring and neutrophil tracking in zebrafish using a 10×/0.3 NA**
 432 **objective lens. a.** fDPC image of zebrafish. **b.** WF and OS-SIM images within the white dashed box in **a**,
 433 reflecting the structure of the heart. **ba:** arterial bulb, **at:** atrium, **ve:** ventricle. **c.** fDPC images of zebrafish at
 434 different time points reflect changes in heartbeat. **d.** (Top) Change in fluorescence intensity in the cardiac region
 435 over time. (Bottom) Significant difference in intensity distribution between diastole and systole after
 436 photobleaching correction. **e.** Observation of neutrophil movement in zebrafish using fluorescence intensity
 437 distribution images captured by OS-SIM. The yellow arrows indicate the tracked neutrophils. **f.** Statistical
 438 analysis of neutrophil movement trajectories and movement speed. The emission centre wavelength is 610 nm.

439

Neutrophil recruitment to the sites of tissue injury typically proceeds in three phases:

440 an initial chemotactic response by individual neutrophils to local damage signals,
441 followed by an amplified migratory wave from distal tissues, ultimately culminating in
442 the collective accumulation of neutrophils at the injury site⁴⁵. However, the intrinsic
443 thickness of the zebrafish larvae introduces a substantial out-of-focus background. To
444 overcome this challenge and enable the accurate tracking of neutrophils, we employed
445 the OS-SIM mode in MFPM. This approach enabled us to resolve neutrophil dynamics
446 in real-time within live specimens. In the fluorescence image shown in Fig. 5e, cells
447 exhibiting a higher fluorescence intensity correspond to labelled neutrophils. Within
448 the observed 4 s timeframe, the neutrophils exhibited rapid migration behaviour, with
449 fluorescence signals displaying irregular spatial distributions over time, forming
450 elongated or arc-like trailing shapes along the migration path. These dynamic
451 morphological features are consistent with known neutrophil behaviour, which requires
452 flexible deformation of the cell body and nucleus to quickly migrate through very
453 narrow endothelial channels to enter tissues^{43, 46}. In addition, the movement trajectory
454 of the neutrophils can be quickly restored by cell tracking, as shown in Fig. 5f, which
455 provides the spatial distribution and pathological conditions of biological tissues.
456 Quantitative analysis revealed that, compared with its initial position at 0 s, the
457 neutrophil reached a maximum displacement of 0.23 mm and an instantaneous peak
458 velocity of 1.03 $\mu\text{m}/\text{ms}$. The maximum component velocities in the x and y directions
459 were 0.92 and 0.46 $\mu\text{m}/\text{ms}$, respectively. At 4 s, a rapid decrease in neutrophil volume
460 was observed, suggesting that the cells entered the injury site to participate in
461 subsequent tissue repair and pathogen clearance.

462 Currently, the precise kinetic mechanisms governing the extravascular migration of
463 neutrophils toward sites of tissue injury remain incompletely understood⁴³. To address
464 this knowledge gap, our MFPM system provides a unique multimodal decision-support
465 capability. By dynamically switching to DPC imaging during neutrophil tracking
466 experiments, researchers can perform real-time physiological state assessments of
467 zebrafish hosts. When a large number of neutrophils undergo directional migration,
468 DPC imaging of the suspected target region enables the instantaneous evaluation of

469 potential inflammatory or pathological changes through quantitative phase signatures.
470 On-demand correlative imaging is an effective technique for identifying occult tissue
471 injury or infection sites that may not yet exhibit overt fluorescence markers. To further
472 demonstrate the ability of the system to capture dynamic quantitative phase variations,
473 we conducted phase monitoring of the L929 cell death dynamics using DPC imaging
474 (Fig. S16). For more detailed information, please refer to [Supplementary Note 8](#).

475 Discussion

476 In this paper, we propose an integrated multimodal fluorescence-phase microscopy
477 (MFPM) system that is capable of fluorescence, polarisation, and phase imaging from
478 the same sample region. The system achieves multimodal capabilities through a unified
479 hardware implementation and computationally efficient reconstruction algorithms,
480 including OS-SIM, SR-SIM, fluorescence polarisation resolving, fDPC, and qDPC
481 imaging. Compared to existing multimodal systems⁴⁷⁻⁵⁰, this system features lower
482 hardware complexity^{47,50}, no additional image registration, and fewer original images^{47,}
483 ⁴⁹. To further enhance the imaging performance, we implemented frame-reduction and
484 background removal strategies, as well as a fluorescence polarisation orientation-
485 resolving algorithm for resolving fluorescence polarisation orientations, enabling
486 access to richer biological information. Experimental validation across diverse
487 biological specimens of varying scales confirmed the broad applicability of MFPM and
488 demonstrated its potential for comprehensive multiscale biological investigations. In
489 U2OS cells, MFPM resolved global cellular topography, SR actin structures, and
490 polarisation-resolved orientation mapping, thereby achieving multidimensional
491 characterisation. For pathological samples, high-throughput screening of DPC imaging,
492 combined with fluorescence intensity analysis and cell nucleus quantitative statistics,
493 has enabled a quantitative auxiliary diagnostic method to distinguish cervicitis from
494 cervical cancer. During the imaging of zebrafish larvae, heart rate metrics were
495 quantitatively assessed via fluorescence and phase verification, whereas the migration
496 of neutrophils was dynamically tracked, with further analysis of their morphological
497 changes and migration speed. The paradigm of high-throughput DPC screening

498 followed by targeted fluorescence observation is expected to become a prominent trend
499 in future imaging applications. This integrated system and workflow offers a flexible,
500 efficient, and information-rich solution for advanced biological and biomedical
501 research, enabling multidimensional data acquisition within a single platform.

502 Although the current implementations have achieved high-quality fluorescence
503 and phase reconstruction, future improvements will further enhance automation and
504 scalability. For instance, combining deep learning with physical knowledge can yield
505 ultrafast noise-robust image reconstruction⁵¹. More accurate physical modeling⁵² or 3D
506 extensions⁵³ can improve the phase retrieval in thick tissues. Meanwhile, virtual
507 staining^{54,55} from phase images can reduce the reliance on labelling and phototoxicity⁵⁶,
508 ⁵⁷. Crucially, the capability of MFPM to rapidly screen large fields and validate targets
509 at high resolution lays the foundation for intelligent event-triggered imaging, enabling
510 real-time, selective capture of dynamic biological processes^{9, 58}. Its common-path
511 design ensures compatibility with 3D volumetric imaging⁵⁹. By combining GPU
512 acceleration and systematic optimisation of the algorithm, the reconstruction speed is
513 expected to be further improved in future work, thereby significantly enhancing the
514 overall capabilities of the system. These features make the MFPM a promising and
515 scalable solution for next-generation automated and intelligent bioimaging.

516 **Acknowledgements**

517 This work was supported by the National Natural Science Foundation of China
518 (62025501 and 92150301 to P. X., 62335008 and 62405010 to M. L., 624B2009 to R.
519 C.), Major Basic Research Project of the Natural Science Foundation of Shandong
520 Province (ZR2024ZD27 to X. S. and P. X.), and the National Key R&D Program of
521 China (2022YFC3401100 to P. X.).

522 **Author contribution**

523 P. X. and M. L. supervised the project. W. W., S. Z., R. C., M. L. and P. X. initiated
524 and conceived the research. S. Z., W. W. and R. C. conducted the MFPM system. R. C.
525 and W. W. developed the reconstruction algorithm. X. B. helped with zebrafish culture.

526 S. G. and Y. F. helped with cell culture. X. S. and Q. L. contributed to the discussion of
527 the manuscript's structure. W. W., S. Z., R. C., M. L. and P. X. wrote the manuscript
528 with input from all authors.

529 **Data and code availability**

530 The reconstruction algorithms associated with this work are available at
531 <https://github.com/MFPM0/MFPM>.

532 **Conflict of interest**

533 The authors declare no competing interests.

534 **Reference**

- 535 1. Hobson, C. M. & Aaron, J. S. Combining multiple fluorescence imaging
536 techniques in biology: when one microscope is not enough. *Molecular Biology*
537 *of the Cell* **33**, tp1 (2022).
- 538 2. Wang, H. D. et al. Deep learning enables cross-modality super-resolution in
539 fluorescence microscopy. *Nature Methods* **16**, 103-110 (2019).
- 540 3. Bullen, A. Microscopic imaging techniques for drug discovery. *Nature Reviews*
541 *Drug Discovery* **7**, 54-67 (2008).
- 542 4. Dhawan, A. P., D'Alessandro, B. & Fu, X. L. Optical imaging modalities for
543 biomedical applications. *IEEE Reviews in Biomedical Engineering* **3**, 69-92
544 (2010).
- 545 5. Ma, J. et al. The multimodality cell segmentation challenge: toward universal
546 solutions. *Nature Methods* **21**, 1103-1113 (2024).
- 547 6. Walter, A. et al. Correlated multimodal imaging in life sciences: expanding the
548 biomedical horizon. *Frontiers in Physics* **8**, 47 (2020).
- 549 7. Liang, Q. X. et al. High-fidelity tissue super-resolution imaging achieved with
550 confocal² spinning-disk image scanning microscopy. *Light: Science &*
551 *Applications* **14**, 260 (2025).
- 552 8. Boutros, M., Heigwer, F. & Laufer, C. Microscopy-based high-content
553 screening. *Cell* **163**, 1314-1325 (2015).
- 554 9. Stepp, W. L. et al. Smart hybrid microscopy for cell-friendly detection of rare
555 events. *Nature Communications* **17**, 1423 (2026).
- 556 10. Qian, J. M. et al. Structured illumination microscopy based on principal
557 component analysis. *eLight* **3**, 4 (2023).
- 558 11. Qian, J. M. et al. Ensemble deep learning-enabled single-shot composite

- 559 structured illumination microscopy (eDL-cSIM). *PhotonIX* **6**, 13 (2025).
- 560 12. Gustafsson, M. G. L. Surpassing the lateral resolution limit by a factor of two
561 using structured illumination microscopy: SHORT COMMUNICATION.
562 *Journal of Microscopy* **198**, 82-87 (2000).
- 563 13. Cao, R. J. et al. Open-3DSIM: an open-source three-dimensional structured
564 illumination microscopy reconstruction platform. *Nature Methods* **20**, 1183-
565 1186 (2023).
- 566 14. Chen, X. et al. Superresolution structured illumination microscopy
567 reconstruction algorithms: a review. *Light: Science & Applications* **12**, 172
568 (2023).
- 569 15. Wang, H. et al. High-spatiotemporal-resolution structured illumination
570 microscopy: principles, instrumentation, and applications. *Photonics Insights* **4**,
571 R01 (2025).
- 572 16. Fu, Y. Z. et al. Triangle-beam interference structured illumination microscopy.
573 *Nature Photonics* **19**, 1122-1131 (2025).
- 574 17. Jiang, S. et al. Frequency-domain diagonal extension imaging. *Advanced*
575 *Photonics* **2**, 036005 (2020).
- 576 18. Mo, Y. Q. et al. Quantitative structured illumination microscopy via a physical
577 model-based background filtering algorithm reveals actin dynamics. *Nature*
578 *Communications* **14**, 3089 (2023).
- 579 19. Jin, L. H. et al. Deep learning enables structured illumination microscopy with
580 low light levels and enhanced speed. *Nature Communications* **11**, 1934 (2020).
- 581 20. Hamilton, D. K. & Sheppard, C. J. R. Differential phase contrast in scanning
582 optical microscopy. *Journal of Microscopy* **133**, 27-39 (1984).
- 583 21. Mehta, S. B. & Sheppard, C. J. R. Quantitative phase-gradient imaging at high
584 resolution with asymmetric illumination-based differential phase contrast.
585 *Optics Letters* **34**, 1924 (2009).
- 586 22. Liu, Z. J. et al. Real-time brightfield, darkfield, and phase contrast imaging in a
587 light-emitting diode array microscope. *Journal of Biomedical Optics* **19**, 1
588 (2014).
- 589 23. Tian, L. & Waller, L. Quantitative differential phase contrast imaging in an LED
590 array microscope. *Optics Express* **23**, 11394-11403 (2015).
- 591 24. Cao, R. J. et al. Dark-based optical sectioning assists background removal in
592 fluorescence microscopy. *Nature Methods* **22**, 1299-1310 (2025).
- 593 25. Ren, W. et al. Expanding super-resolution imaging versatility in organisms with
594 multi-confocal image scanning microscopy. *National Science Review* **11**,
595 nwae303 (2024).

- 596 26. Lal, A. et al. A frequency domain SIM reconstruction algorithm using reduced
597 number of images. *IEEE Transactions on Image Processing* **27**, 4555-4570
598 (2018).
- 599 27. Chen, M., Phillips, Z. F. & Waller, L. Quantitative differential phase contrast
600 (DPC) microscopy with computational aberration correction. *Optics Express* **26**,
601 32888-32899 (2018).
- 602 28. Lim, D., Chu, K. K. & Mertz, J. Wide-field fluorescence sectioning with hybrid
603 speckle and uniform-illumination microscopy. *Optics Letters* **33**, 1819-1821
604 (2008).
- 605 29. Philipp, K. et al. Volumetric HiLo microscopy employing an electrically tunable
606 lens. *Optics Express* **24**, 15029-15041 (2016).
- 607 30. Zhanghao, K. et al. Super-resolution imaging of fluorescent dipoles via
608 polarized structured illumination microscopy. *Nature Communications* **10**, 4694
609 (2019).
- 610 31. Zhanghao, K. et al. High-dimensional super-resolution imaging reveals
611 heterogeneity and dynamics of subcellular lipid membranes. *Nature*
612 *Communications* **11**, 5890 (2020).
- 613 32. Zhong, S. Y. et al. Three-dimensional dipole orientation mapping with high
614 temporal-spatial resolution using polarization modulation. *PhotonIX* **5**, 12
615 (2024).
- 616 33. Koho, S. et al. Fourier ring correlation simplifies image restoration in
617 fluorescence microscopy. *Nature Communications* **10**, 3103 (2019).
- 618 34. Thekkek, N. & Richards-Kortum, R. Optical imaging for cervical cancer
619 detection: solutions for a continuing global problem. *Nature Reviews Cancer* **8**,
620 725-731 (2008).
- 621 35. Castellanos, M. R. et al. Diagnostic imaging of cervical intraepithelial neoplasia
622 based on hematoxylin and eosin fluorescence. *Diagnostic Pathology* **10**, 119
623 (2015).
- 624 36. Fuchs, E. Keratins as biochemical markers of epithelial differentiation. *Trends*
625 *in Genetics* **4**, 277-281 (1988).
- 626 37. Pachitariu, M., Rariden, M. & Stringer, C. Cellpose-SAM: superhuman
627 generalization for cellular segmentation. *bioRxiv* (2025).
- 628 38. Ling, D. M. et al. Quantitative measurements of zebrafish heart rate and heart
629 rate variability: a survey between 1990-2020. *Computers in Biology and*
630 *Medicine* **142**, 105045 (2022).
- 631 39. Teixidó, E. et al. Automated morphological feature assessment for zebrafish
632 embryo developmental toxicity screens. *Toxicological Sciences* **167**, 438-449

- 633 (2019).
- 634 40. Pylatiuk, C. et al. Automatic zebrafish heartbeat detection and analysis for
635 zebrafish embryos. *Zebrafish* **11**, 379-383 (2014).
- 636 41. Lowe, D. G. Distinctive image features from scale-invariant keypoints.
637 *International Journal of Computer Vision* **60**, 91-110 (2004).
- 638 42. Sampurna, B. P. et al. A simple ImageJ-based method to measure cardiac rhythm
639 in zebrafish embryos. *Inventions* **3**, 21 (2018).
- 640 43. Myllymäki, H., Yu, P. Y. & Feng, Y. Opportunities presented by zebrafish larval
641 models to study neutrophil function in tissues. *The International Journal of*
642 *Biochemistry & Cell Biology* **148**, 106234 (2022).
- 643 44. Herrero-Cervera, A., Soehnlein, O. & Kenne, E. Neutrophils in chronic
644 inflammatory diseases. *Cellular & Molecular Immunology* **19**, 177-191 (2022).
- 645 45. Ng, L. G. et al. Visualizing the neutrophil response to sterile tissue injury in
646 mouse dermis reveals a three-phase cascade of events. *Journal of Investigative*
647 *Dermatology* **131**, 2058-2068 (2011).
- 648 46. Manley, H. R., Keightley, M. C. & Lieschke, G. J. The neutrophil nucleus: an
649 important influence on neutrophil migration and function. *Frontiers in*
650 *Immunology* **9**, 2867 (2018).
- 651 47. Dong, D. S. et al. Super-resolution fluorescence-assisted diffraction
652 computational tomography reveals the three-dimensional landscape of the
653 cellular organelle interactome. *Light: Science & Applications* **9**, 11 (2020).
- 654 48. Ma, Y. et al. Label-free imaging of intracellular organelle dynamics using flat-
655 fielding quantitative phase contrast microscopy (FF-QPCM). *Optics Express* **30**,
656 9505-9520 (2022).
- 657 49. Wen, K. et al. Structured illumination microscopy with partially coherent
658 illumination for phase and fluorescent imaging. *Optics Express* **29**, 33679-
659 33693 (2021).
- 660 50. Wen, K. et al. Structured illumination phase and fluorescence microscopy for
661 bioimaging. *Applied Optics* **62**, 4871-4879 (2023).
- 662 51. Qiao, C. et al. Rationalized deep learning super-resolution microscopy for
663 sustained live imaging of rapid subcellular processes. *Nature Biotechnology* **41**,
664 367-377 (2023).
- 665 52. Fan, Y. et al. Accurate quantitative phase imaging by differential phase contrast
666 with partially coherent illumination: beyond weak object approximation.
667 *Photonics Research* **11**, 442-455 (2023).
- 668 53. Chen, M., Tian, L. & Waller, L. 3D differential phase contrast microscopy.
669 *Biomedical Optics Express* **7**, 3940-3950 (2016).

- 670 54. Park, J. et al. Artificial intelligence-enabled quantitative phase imaging methods
671 for life sciences. *Nature Methods* **20**, 1645-1660 (2023).
- 672 55. Elmalam, N., Ben Nedava, L. & Zaritsky, A. In silico labeling in cell biology:
673 potential and limitations. *Current Opinion in Cell Biology* **89**, 102378 (2024).
- 674 56. Fang, J. D. et al. Label-free analysis of organelle interactions using organelle-
675 specific phase contrast microscopy (OS-PCM). *ACS Photonics* **10**, 1093-1103
676 (2023).
- 677 57. Ivanov, I. E. et al. Mantis: high-throughput 4D imaging and analysis of the
678 molecular and physical architecture of cells. *PNAS Nexus* **3**, pgae323 (2024).
- 679 58. Mahecic, D. et al. Event-driven acquisition for content-enriched microscopy.
680 *Nature Methods* **19**, 1262-1267 (2022).
- 681 59. Li, Y. N. et al. High-speed autopolarization synchronization modulation three-
682 dimensional structured illumination microscopy. *Advanced Photonics Nexus* **3**,
683 016001 (2024).